Complex spin texture of Dirac cones induced via spin-orbit proximity effect in graphene on metals

Jagoda Sławińska[1,2,3,*] and Jorge I. Cerdá[1]

[1]*Instituto de Ciencia de Materiales de Madrid, ICMM-CSIC, Cantoblanco, 28049 Madrid, Spain*

[2]*Department of Solid State Physics, University of Łódź, Pomorska 149/153, 90236 Łódź, Poland*

[3]*Consiglio Nazionale delle Ricerche, Istituto SPIN L'Aquila, sede temporanea di Chieti, 66100 Italy*

(Received 31 October 2017; published 30 August 2018)

We use large-scale DFT calculations to investigate with unprecedented detail the so-called spin-orbit (SO) proximity effect in graphene adsorbed on the Pt(111) and Ni(111)/Au semi-infinite surfaces, previously studied via spin and angle resolved photoemission (SP-ARPES) experiments. The key finding is that, due to the hybridization with the metal's bands, the Dirac cones manifest an unexpectedly rich spin texture including out-of-plane and even radial in-plane spin components at (anti)crossings where local gap openings and deviations from linearity take place. Both the continuum character of the metallic bands and the back folding associated to the moiré patterns enhance the spin texture and induce sizable splittings which, nevertheless, only become giant (∼100 meV) at anticrossing regions; that is, where electronic transport is suppressed. At the quasilinear regions the splitted bands typically disperse with different broadenings and tend to cross with their magnetization continuously changing in order to match that at the edges of the upper and lower gaps. As a result, both the splittings and spin direction become strongly k dependent. The SO manifests in an analogous way for the spin-polarized G/Au/Ni(111) system, although here the magnetic exchange interactions dominate inducing small splittings (∼10 meV) in the π bands while the SO mainly introduces a small Rashba splitting in the Dirac cones as their magnetization acquires a helical component. While revealing such complex spin texture seems challenging from the experimental side, our results provide an important reference for future SP-ARPES measurements of similar graphene based systems extensively investigated for applications in spintronics.

DOI: 10.1103/PhysRevB.98.075436

I. INTRODUCTION

Spin-orbit coupling (SOC) in graphene [1] has been proposed as a basis for various phenomena of fundamental and practical importance for spintronics, such as the spin Hall effect [2,3], topological quantum spin Hall effect (QSHE) [4], quantum anomalous Hall effect (QAHE) [5,6], weak localization [7], or electron confinement associated to multiple topologically nontrivial gaps [8]. Given the tiny intrinsic SOC of graphene (G), estimated to be less than few tens of μeV [9,10], which makes the experimental realization of such phenomena unfeasible, extensive efforts have been devoted to find an efficient way to enhance and tune the strength of SOC extrinsically. One of the most promising approaches is the so-called proximity effect [11–14] whereby the large SOC of heavy elements either adsorbed or present in the substrate may be transferred to the G, as can be explained in terms of diverse hopping processes onto and off the metal atoms so that the electron acquires a large SOC before it returns to the graphene [13]. For any practical purposes, however, a straightforward and robust approach for SOC engineering is of vital importance. Epitaxial graphene grown on metallic surfaces seems to be an excellent candidate to achieve this goal, mainly due to an easy fabrication process and absence of a structural disorder which could deteriorate the spin and charge transport performance. Notably, metallic substrates also offer a chance to adsorb or intercalate atoms/layers providing a plethora of options for further tuning other relevant properties apart from solely changing the strength of SOC [8,15].

Despite continuous experimental attempts performed during the last years in order to achieve strong spin-orbit proximity effect in graphene [3,8,11,16–22], the corresponding theoretical studies are rather scarce and involve oversimplified models mainly due to the large computational resources that the inclusion of SOC requires. Typically, these works are restricted to either diluted metallic layers or slabs with small unit cells which cannot appropriately take into account the commensurability between graphene layer and the underlying substrate. In fact, a realistic *ab initio* modeling of SOC-related phenomena in graphene/metal interfaces has been missing so far. In this paper we fill this gap by addressing, from a theoretical perspective, the fundamental question of how a semi-infinite metallic substrate alters the graphene's Dirac cones (DCs) and determines their spin texture. We consider graphene/metal interfaces involving large supercells thus reducing artificial strains typically imposed when oversimplified commensurabilities are assumed. Therefore, our approach introduces a further source of graphene/metal hybridization due to the Brillouin zone (BZ) backfolding whose impact, as shown below, is by no means negligible. We analyze two different examples of metallic substrates: a Pt(111) surface and a Au monolayer adsorbed on a Ni(111) surface, the choice being motivated by several spin- and angle-resolved

*Present address: Department of Physics, University of North Texas, Denton, Texas 76203, USA.

photoemission spectroscopy (SP-ARPES) measurements where large Rashba splittings (RS) of up to ∼100 meV have been reported for both systems [16–19] as well as by the fact they present fundamental differences in their electronic properties. The former involves π-d interactions between the graphene and the Pt and, being nonmagnetic, preserves the Kramer's degeneracy. It thus represents an ideal system to estimate the SOC derived splittings by inspecting the spin structure of the Dirac cone states. In contrast, the G-Au interactions are mainly of the π-sp type and, more interestingly, the gold layer shows a net magnetization due to the presence of the ferromagnetic substrate below which constitutes an excellent playground to explore the interplay between SOC and spin-exchange derived splittings [23]. Furthermore, the same group has reported the co-existence of two phases for this system showing small and large splittings [17], although the origin of such a puzzling difference could not be confirmed. Throughout, we focus on the induced spin texture of the Dirac cones rather than on any topological properties that could emerge at opened gaps (due to intrinsic SOC [4,13]) since we are primarily interested on the spin properties of the linear π bands. It turns out that the key mechanism behind the transfer of SOC to the G's π bands is hybridization with the surface localized metal d states which hold the largest SOC derived spin splittings. It is precisely at such (anti)crossings where minigaps are opened and the DCs show the largest distortions attaining band splittings above 100 meV. On the other hand, in the absence of strong hybridizations (regions of highly dispersive sp metal bands) the influence of the SOC on the G is minor and the splittings are at most a few tens of meV.

The paper is organized as follows: In Sec. II we discuss the details of the DFT and Green's functions calculations. Section III is devoted to the origin and peculiarities of the spin texture induced in graphene's Dirac cones by a Pt(111) substrate. In Sec. IV the interplay between SOC and magnetic order in G/Au/Ni(111) is examined, while in Sec. V we summarize the main conclusions and perspectives.

II. METHODS

Our density functional theory (DFT) based calculations were performed with the GREEN code [24,25] employing an interface to the *ab initio* SIESTA package [26]. The exchange-correlation (XC) interaction was treated under the generalized gradient approximation (GGA) following the parametrization of Perdew, Burke, and Ernzerhof [27], including spin polarization in all cases where Ni atoms were involved. Dispersion forces were taken into account via the semiempirical scheme of Ortmann and Bechstedt [28]. The fully-relativistic pseudopotential (FR-PP) formalism [29] was employed to account for the SOC. Core electrons were replaced by norm-conserving pseudopotentials of the Troulliers-Martin type, with core corrections included for the metal atoms in order to better describe the XC and SOC terms [29]. The atomic orbital (AO) basis set consisted of double-zeta polarized (DZP) numerical orbitals strictly localized—we set the confinement energy to 100 meV. Real space three-center integrals were computed over 3D grids with a resolution of ∼0.07 Å^3—equivalent to 500 Rydbergs mesh cutoff. Brillouin zone integration was performed over k supercells of around (18×18) relative to the G-(1×1) lattice.

All considered graphene/metal structures were first relaxed employing two-dimensional periodic slabs involving several metal layers and the graphene on top. In the case of G/Pt(111) we considered six Pt layers thick slabs and two different moiré patterns, the so-called (2×2) and (3×3) phases [30–32], described in detail in Sec. III. On the other hand, and based on previous studies on the Au/Ni(111) surface [33], we modeled the G/Au/Ni system assuming a (9×9)/(8×8)/(9×9) commensurability between the G, Au, and Ni lattices, respectively, with the Au layer intercalated between the G and a four Ni layers thick slab. Two different phases were considered: one, where the Ni surface is unreconstructed and a second one, where the top Ni layer presents a large triangular reconstruction [33]—its precise geometrical description is given in Appendix C. In all cases the graphene atoms and the first two metallic layers were allowed to relax until forces were below 0.03 eV/Å while the bottom layers (four in the case of Pt and two for Au/Ni) were held fixed to bulk positions.

G adsorption energies were computed as the balance between the total energy of the system and that of the sum of the clean relaxed metal surface and freestanding G. However, although the semiempirical vdW approach followed here is necessary to obtain the correct adsorption geometries, it largely overestimates adsorption energies [34]. Hence, we have estimated these energies after removing all vdW contributions [35].

The electronic structure for the semi-infinite surfaces was computed following several steps. Once the structures described above were optimized, we added four (one) bulklike layers of Pt (Ni) at the bottom of the slabs and recomputed their Hamiltonians self-consistently first neglecting and next including SOC (see Ref. [29] for full details of the implementation). In the last step, we used the appropriate Hamiltonian matrix elements to stack the graphene and first metallic layers on top of bulk Pt(111) and Ni(111) semi-infinite blocks via Green's functions matching techniques following the prescription detailed elsewhere [25,36].

Since for a semi-infinite system the absence of translational symmetry along the surface normal does not allow us to evaluate the band structure via the diagonalization of the Hamiltonian matrix, we compute instead equivalent k-resolved density of states projected on different surface atoms, PDOS($\vec{k}$, E). For a particular layer I, its DOS projection is calculated from the system Green's function blocks, G_{IJ}, connecting I with itself and its neighbor layers J, according to:

$$PDOS_I(\vec{k}, E) = \frac{-i}{\pi} \sum_{\sigma, J} Tr\left\{G^{\sigma\sigma}_{IJ}(\vec{k}, E)\; O_{JI}(\vec{k})\right\}, \qquad (1)$$

where $\sigma = \uparrow, \downarrow$ denotes the spin component and $O_{IJ}(\vec{k})$ stands for the k-space overlap between layers I and J. The summation over J only includes layers $I-1$, I, and $I+1$ because all layers are defined thick enough so that overlap matrices beyond first nearest neighbor layers vanish (obviously, for the surfacemost layer only the I and $I-1$ terms will enter the above equation).

Similarly, k-resolved magnetization densities, $\vec{m}(\vec{k}, E)$, may be obtained as:

$$m_x(\vec{k}, E) = \frac{-2i}{\pi} \sum_J Tr\{G_{IJ}^{\uparrow\downarrow}(\vec{k}, E)\ O_{JI}(\vec{k})\} \quad (2)$$

$$m_y(\vec{k}, E) = \frac{2}{\pi} \sum_J Tr\{G_{IJ}^{\uparrow\downarrow}(\vec{k}, E)\ O_{JI}(\vec{k})\} \quad (3)$$

$$m_z(\vec{k}, E) = \frac{-i}{\pi} \sum_J Tr\{(G_{IJ}^{\uparrow\uparrow}(\vec{k}, E) - G_{IJ}^{\downarrow\downarrow}(\vec{k}, E))O_{JI}(\vec{k})\}. \quad (4)$$

In this paper, we will present most of our results in the form of $(\vec{k}, E)$ maps projected either on the G or the metal layers. Furthermore, most of the G and first Pt layer projections have been computed within the moiré supercell (folded electronic/magnetic structures) as well as assuming that translational (1×1) symmetry is preserved within the layer (unfolded structures) following the approach described in Appendix A. For all $(\vec{k}, E)$ maps we have typically employed a resolution of ∼6×10^{-3} Å^{-1} in k space and 1–2 meV in energy while the imaginary part of the energy entering the Green's function calculation (self-energy or broadening) was accordingly set to 2–4 meV. These small values ensure that the widths of the peaks in the calculated G PDOS arise from the metal's self-energy (i.e., the interaction with the continuum of metal bands). We note that such a high resolution required a huge computational effort, as the maps presented in this work typically comprised of the order of 10^6 and 10^5 $(\vec{k}, E)$ grid points for the G/Pt and G/Au/Ni systems, respectively.

III. GRAPHENE ON PT(111)

Out of the over 20 different moiré patterns reported for this system [30,32], we considered the two most common phases namely, $(2\times2)/(\sqrt{3}\times\sqrt{3})R30°$ and $(3\times3)/(\sqrt{7}\times\sqrt{7})R19.1°$—hereafter denoted as (2×2) and (3×3), respectively. As described above, both were modeled placing a graphene sheet on top of a Pt(111) slab and fixing the Pt bulk lattice constant to its experimental value, $a_{Pt} = 3.92$ Å, leading to G's lattice constants of $a_G = 2.40$ and 2.44 Å for the (2×2) and (3×3) supercells, respectively. Whereas the former represents a noticeable 2.5% compression with respect to pristine G, the latter is only 0.8% smaller than the experimental value of 2.46 Å. In Fig. 1(a) we show the optimized geometries, for which we obtained an uncorrugated G layer adsorbed at 3.33 and 3.36 Å from the Pt surface, in good agreement with the 3.3 Å distance obtained experimentally [37]. Energetically, the (3×3) phase was found marginally more stable than the (2×2), with adsorption energies (see section Methods) of 26 and 23 meV/C, respectively, both clearly in the physisorption regime [38].

Figure 1(b) sketches the 2D reciprocal space for both phases with the G and Pt BZs indicated in green and blue, respectively, and that of the commensurate supercell in red in an extended zone scheme. Whereas in the (2×2) case the K_G and K'_G high-symmetry points are backfolded into the supercell's BZ K' and K points, for the (3×3) they all transform into the Γ point. Nevertheless, the quasifreestanding character of the graphene

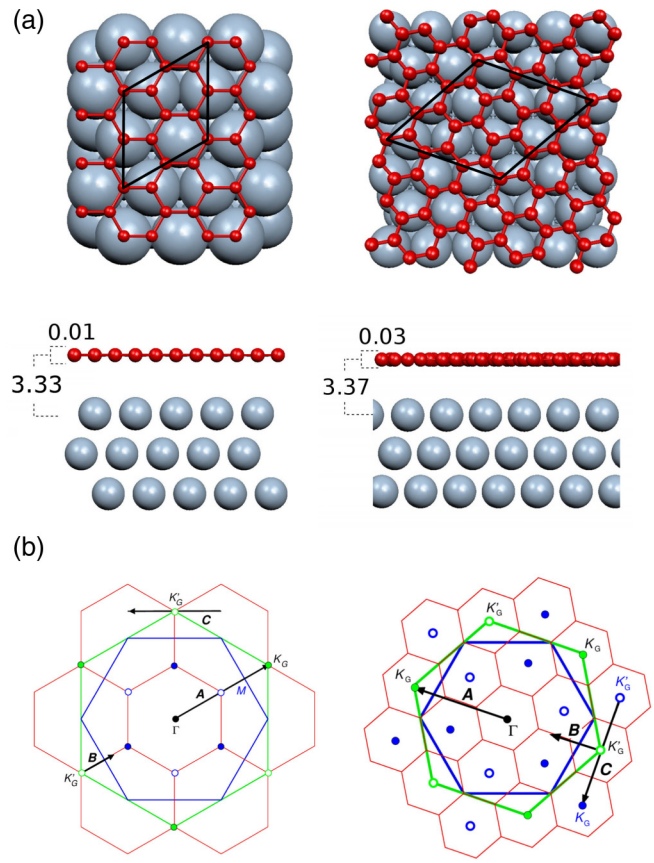

FIG. 1. (a) Top and side views of the G-(2×2)/$(\sqrt{3}\times\sqrt{3})R30°$ (left-hand panel) and G-(3×3)/Pt(111)-$(\sqrt{7}\times\sqrt{7})R19.1°$ (right-hand panel) configurations. C and Pt atoms are represented by small red and large blue balls, respectively. The commensurate supercells are indicated by the parallelograms. In the side views the optimized Pt-G interlayer distance and the G's intralayer corrugation are given in Å. (b) Corresponding combined BZ schemes for each phase. Small red hexagons correspond to the G's folded BZ—(2×2) at the left and (3×3) at the right, while larger blue and green hexagons correspond to the Pt(111) and G's primitive BZs, respectively. Closed/open blue circles mark the G's K_G/K'_G points including those backfolded into the Pt's primitive BZ. Black arrows indicate the k lines A, B, and C.

layer allows us to accurately unfold the PDOS$(\vec{k}, E)$ and $\vec{m}(\vec{k}, E)$ quantities onto its primitive BZ and, hence, examine the π-band dispersion and spin texture around K_G and K'_G separately (see Appendix A). Similarly, the scarce reconstruction of the Pt topmost layers permits an analogous unfolding but onto the Pt(111)-(1×1) BZ. We have computed the electronic structure for k lines running along the $\Gamma - K_G/K'_G$ direction [paths A and B in Fig. 1(b)] and a third line passing through K'_G but perpendicular to the previous ones (path C).

Since the (2×2) phase is the most simple and symmetric one, we will first present a very detailed study for this phase in order to establish the main mechanisms dictating the G's induced spin texture; as shown in the next subsections, most of them still hold for the (3×3) case.

A. (2×2) phase

Figure 2(a) presents the unfolded electronic dispersion PDOS$(\vec{k}, E)$ for the (2×2) phase projected on the first two Pt

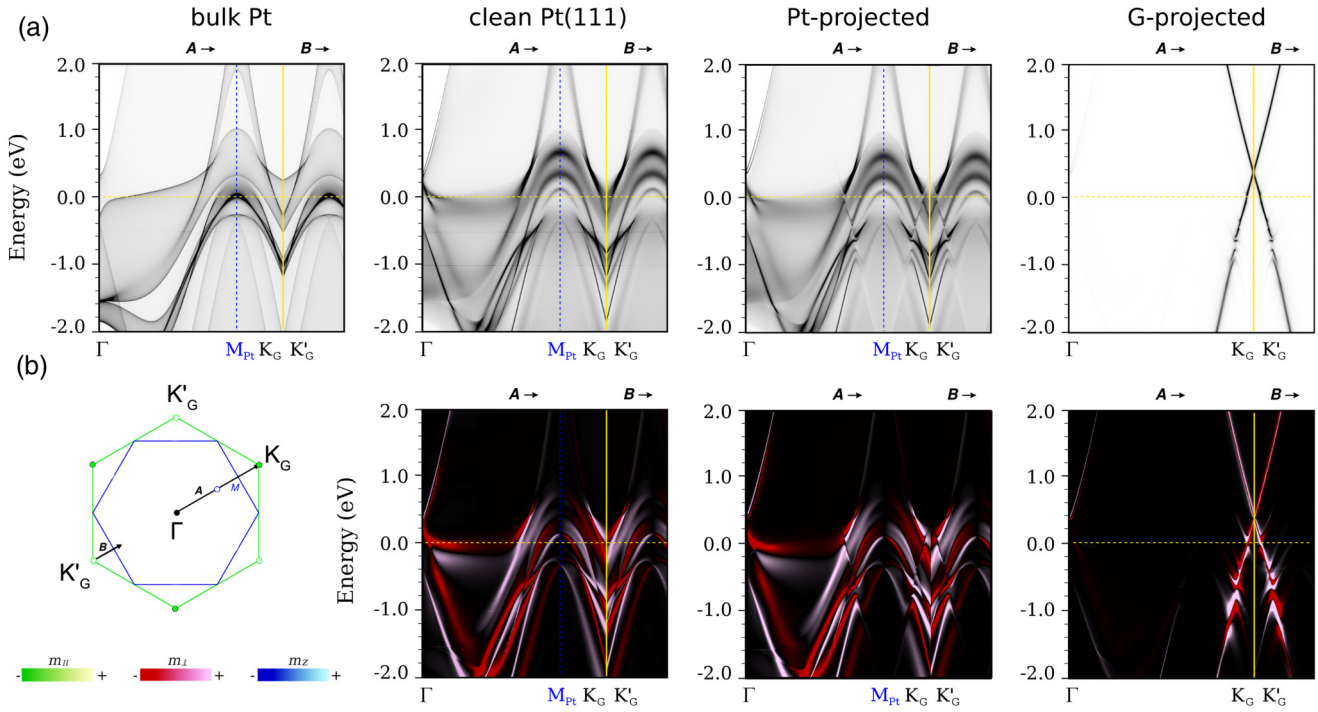

FIG. 2. (a) First column: PDOS($\vec{k}$, E) map of bulk Pt along the A-B k-path defined in the inset below and Fig. 1(b). Second column: Same as first column, but calculated for clean Pt(111)-(1×1) semi-infinite surface and projected on the surface layer. Third column: PDOS($\vec{k}$, E) map calculated for the G-(2×2)/($\sqrt{3}\times\sqrt{3}$)$R30^\circ$ semi-infinite surface and projected on the Pt surface layer along the same A-B k-path after unfolding onto the Pt (1×1) BZ. Last column: Same as third column but projected on the graphene layer after unfolding onto the G's (1×1) BZ. (b) The associated G's magnetization map, $\vec{m}(\vec{k}, E)$, for the same systems and projections as in (a) after superimposing the $\perp$, $\parallel$ and z components, each color coded as indicated by the legends at the bottom left (although only $m_\perp$ is nonzero along these k-paths). The inset on the left shows the primitive BZs of graphene (green) and Pt(111) (blue) and the considered high-symmetry k-paths.

layers and on graphene along the A and B paths (two rightmost columns in the figure). Both paths are displayed side by side because they are related through (2D) inversion symmetry thus yielding symmetric PDOS about the degenerate K_G/K'_G point. For the sake of clarity and completeness, we also show in the two leftmost panels the electronic structure of bulk Pt and the clean Pt(111)-(1×1) surface along the same k lines. The bulk projection shows the expected continuum of d bands mainly covering the occupied states region as well as a prominent bump at the Pt's BZ boundary (point M_{Pt}) raising up to 1 eV. Narrow gap areas appear across $\Gamma - M_{Pt}$ as well as around K_G. The rest of the energy region above the Fermi level, E_F, is filled by a continuum of highly dispersive (less intense) sp-type bands with large gaps emerging from Γ and K_G. At the edges the DOS becomes sharp and intense due to the projection of the bands' curvature along the surface normal. The PDOS($\vec{k}$, E) for the clean surface presents several important differences with respect to its bulk counterpart: a smearing and broadening of the band edges, the appearance of intense surface resonances corresponding to states with a strong 2D character, and the filling of all bulk gaps below E_F. Moreover, a sharp Rashba splitted surface state emerges from Γ with its onset just below 0.4 eV.

The equivalent surface Pt projections computed for the combined G/Pt(111) surface system are essentially the same as for the clean case, except for quasilinear traces belonging to the π bands of graphene which can be seen around K_G/K'_G especially in the d-band region (together with a backfolded replica at the left of M_{Pt}). The PDOS($\vec{k}$, E) projected on graphene reveals that the Dirac cones are essentially preserved, with a strong 0.40 eV p-type doping as a consequence of the compressed C-C distances [39], while no gap is opened between the upper and lower cones signaling a weak intrinsic SOC. Within the 2 meV energy resolution (broadening) employed, no hints for any RS can be seen in the maps but just an overall blurring of the lower cone due to hybridization with the Pt-d bands, as well as a large gap opening at ~ -0.7 eV. The upper cone, on the other hand, appears sharper and closely resembles that of pristine graphene.

Inspection of the spin structure enhances all these features and allows us to examine the SOC induced effects in greater detail. In Fig. 2(b) we present the magnetization dispersion $\vec{m}(\vec{k}, E)$ for the same projections as in (a). The magnetization vector has been decomposed into two in-plane components, one along the k line ($m_\parallel$) and the other one orthogonal to it ($m_\perp$) plus the the out-of-plane contribution (m_z). The $\vec{m}(\vec{k}, E)$ map for the bulk phase is omitted since Kramer's degeneracy $[E(\vec{k}, \sigma) = E(-\vec{k}, \sigma')]$ when combined with the inversion symmetry holding for fcc Pt ($E(\vec{k}, \sigma) = E(-\vec{k}, \sigma)$) forbids any net magnetization in k space—indeed, the computed $\vec{m}(\vec{k}, E)$ map is completely dark. On the other hand, and as expected for a heavy metal surface [40], the clean Pt(111)-(1×1) spin texture is very rich presenting large splittings associated to magnetizations which are always locked along the $m_\perp$ direction

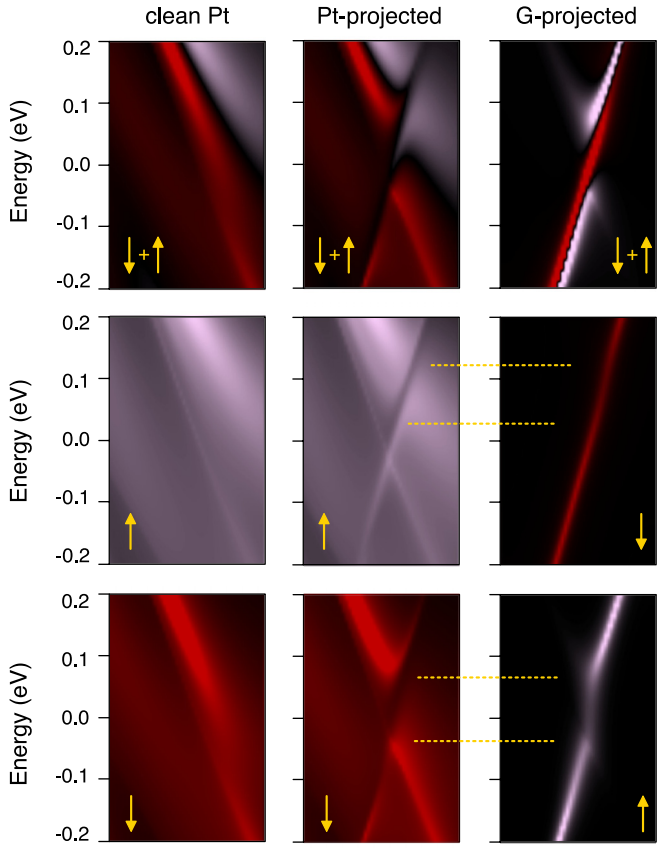

FIG. 3. Top row: zoom in of the magnetization maps shown in Fig. 2(b) in the vicinity of E_F. First column corresponds to the clean Pt(111) surface, and second and third columns to the G and Pt projections, respectively. Middle and bottom rows present a decomposition of the $\vec{m}(\vec{k}, E)$ maps into its ↑ (pink) and ↓ (red) components—see arrows in the inset of each figure. Since the G-Pt coupling in this region is antiferromagnetic, we have placed in each row the G's spin component opposite to that of the Pt. Yellow dashed lines indicate the lower and upper edges of the gaps opened at each spin branch.

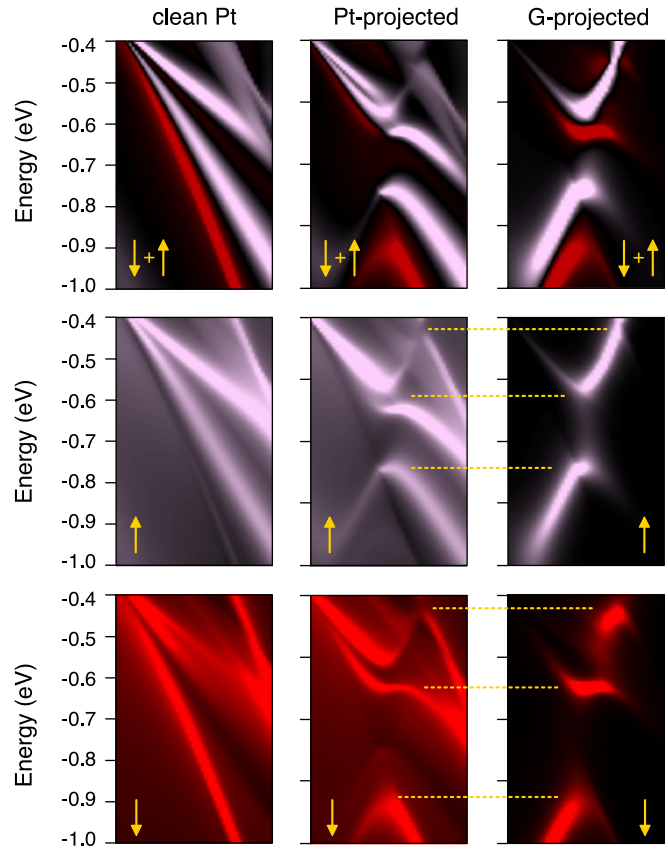

FIG. 4. Similar zooms as in Fig. 3 but taken over a wider energy range below E_F. This time, since the Pt-G coupling is mainly ferromagnetic we have placed the ↑ or ↓ projections for both G and Pt in the same rows.

(only red-pink tones appear in the maps). The spin locking results from the fact that the A and B paths run along a mirror symmetry plane so that the symmetry transformation applying to the $\vec{m}$ *pseudovector*, $\tau(m_\parallel, m_\perp, m_z) = (-m_\parallel, m_\perp, -m_z)$, leads to vanishing $m_\parallel$ and m_z components precisely at the mirror plane. On the other hand, due to Kramer's degeneracy, the Rashba splitted bands are antisymmetric about the time reversal invariant momentum (TRIM) M_{Pt} point, with abrupt inversions of $m_\perp$ occurring at this point. Likewise, the same antisymmetric behavior is found between the A and B paths around the K_G/K'_G points.

The Pt magnetization dispersion hardly changes when the graphene is adsorbed on top, although the traces of Dirac states become more patent and can be identified as minigap openings at the avoided crossings with the Pt's Rashba splitted bands (see below). Notably, the G projection shows an unexpectedly complex spin texture, with the lower cone covered with streaks and undergoing numerous spin flips due to hybridization with the Pt bands while the upper cone appears free of any crossings. Nevertheless, both the Pt and G magnetizations remain locked to the momentum (only $m_\perp$ component) since the mirror symmetry plane is preserved in the combined G/Pt (2×2) phase.

In order to gain insight into the SOC mediated graphene/Pt hybridization mechanism we first examine the energy region where the metallic bands cross the π bands closest to the Dirac point (0.3 eV interval around E_F). A zoom in of this region is presented in Fig. 3, including the Pt and G $\vec{m}(\vec{k}, E)$ projections (second and third columns, respectively) as well as that for the clean Pt surface (first column). We have further decomposed the magnetization into its ↑ and ↓ components with their respective maps appearing in lower rows [to this end, we diagonalized the (2×2) PDOS$^{\sigma\sigma'}$ matrix at each energy and k point]. The clean Pt electronic structure in this region consists of a broad ↑ and an intense and sharper ↓ continuum of bands, the former slightly shifted to the right. In the combined G/Pt system each spin component of graphene interacts with the opposite spin component metal band tearing it after opening a gap across it (marked by the dashed yellow lines). Therefore, the spin coupling in this region is antiferromagnetic. Each π branch itself also opens a ∼100 meV gap as revealed by clear deviations from linearity at the upper and lower gap edges, especially at the G's ↑ branch, which interacts more strongly. Indeed, the gap edges can be clearly resolved in the corresponding Pt projections while a blurred DOS crosses the gap for both graphene's spin components, although at this point

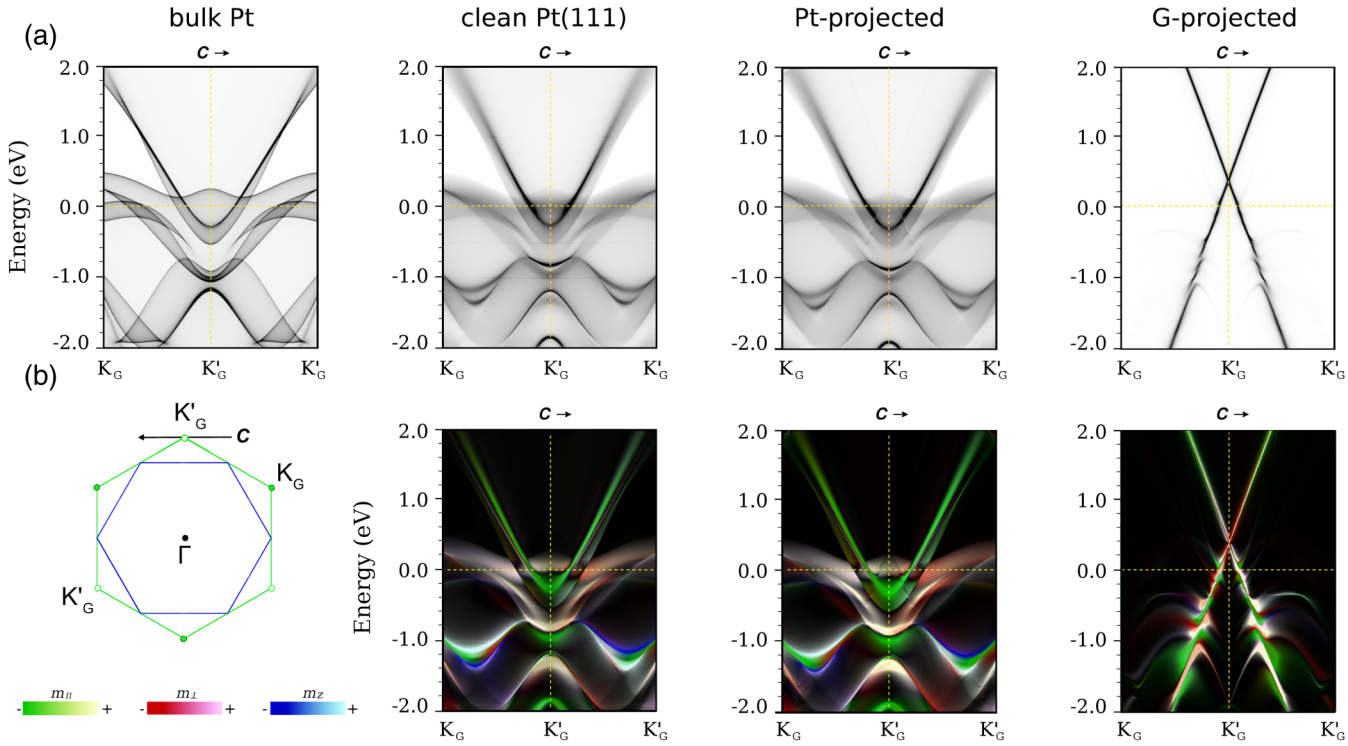

FIG. 5. Same as Fig. 2 but calculated along the direction perpendicular to $\Gamma - K'_G$ (k line C in the inset). To view each spin component independently see Fig. S1 of the Supplemental Material [41].

we cannot discern if it corresponds to a topologically protected state or to slowly decaying evanescent waves or to some type of *partial* hybridization. Due to the Rashba shift between the ↑ and ↓ Pt bands, the location of the gap differs in energy between both spin components by ∼100 meV. The resulting G's magnetization acquires a complex texture; above the gap both spin components run in parallel albeit the ↑ branch is broader and slightly k shifted to the left. Below the avoided crossing, both emerge with similar broadenings but now the ↑ k shifted to the right of the ↓ branch.

Figure 4 displays another zoom in of Fig. 2(b) covering the -1.0 to -0.4 eV energy interval where the π bands undergo the largest distortions. Here the G's ↑ branch interacts with the Pt's leftmost ↑ band (ferromagnetic coupling) opening a large gap of almost 200 meV which is again crossed by a blurred DOS. The G's ↓ branch is however much more textured, as it opens three gaps with vanishing DOS across them. The lower gap edge (around -0.7 eV) arises from the ferromagnetic coupling with the sharp leftmost Pt ↓ branch. Slightly below -0.6 eV a saddle-point feature develops (interband state) which links the ↓ Pt branch at its left with another ↑ band at its right, leaving an abrupt inversion of the magnetization which can be clearly seen in the Pt-projected map at the top row. Another intense G ↓ feature appears at -0.45 eV as a result of the hybridization with the Pt band dispersing at the upper right corner. Since this band is hardly spin polarized (it contains similar ↑ and ↓ contributions) it also hybridizes with the G's ↑ component creating a minigap which can be more clearly seen in the ↑ Pt-projected map.

Once we have shown for the simplest case—spin locked in one direction—that the transfer of SOC from the metal to the G π bands occurs at anticrossing regions and is strongly spin dependent, we next generalize this conclusion to more complex cases by gradually lifting the symmetry constraints. Figure 5 displays 2D maps analogous to those in Fig. 2 but computed along k path C. Since this line is perpendicular to the mirror plane, the magnetization is not constrained along the $\perp$ direction any more and its three components are in general nonzero. They have been simultaneously merged in each frame employing green, red, and blue color scales for $m_\perp$, $m_\parallel$, and m_z, respectively [see color scheme in the legend of Fig. 5(b)]. The last two are antisymmetric about K'_G with abrupt inversions occurring at this point, while the DOS($\vec{k}$, E) and $m_\perp$ component remain symmetric. In the Pt projections an intense parabolic band already present in the bulk (onset from K'_G at ~ -0.3 eV) disperses across the empty states region, while surface resonances appear at the d-band edge crossing E_F and sharp surface d states develop around -1.0 eV where the bulk presents gap areas. They all become more patent in the magnetization maps, which show that the spin is mostly confined in-plane (m_z tends to be smaller) except at the d-band minima located at -1 eV, which acquire a strong out-of-plane character.

Similar to the A-B path, the upper Dirac cone remains almost intact (absence of hybridization with any metallic bands), sharp and hardly splitted within the high 2 meV energy resolution (broadening) employed in our calculations. Its spin remains in-plane ($m_z = 0$) but, at contrast to the previous A-B path, it is not strictly tangential to the cone since the $m_\parallel$ projections do not vanish. The lower cone, on the other hand, is strongly distorted due to multiple anticrossings with the Pt bands. In the PDOS map we can notice two large gaps which

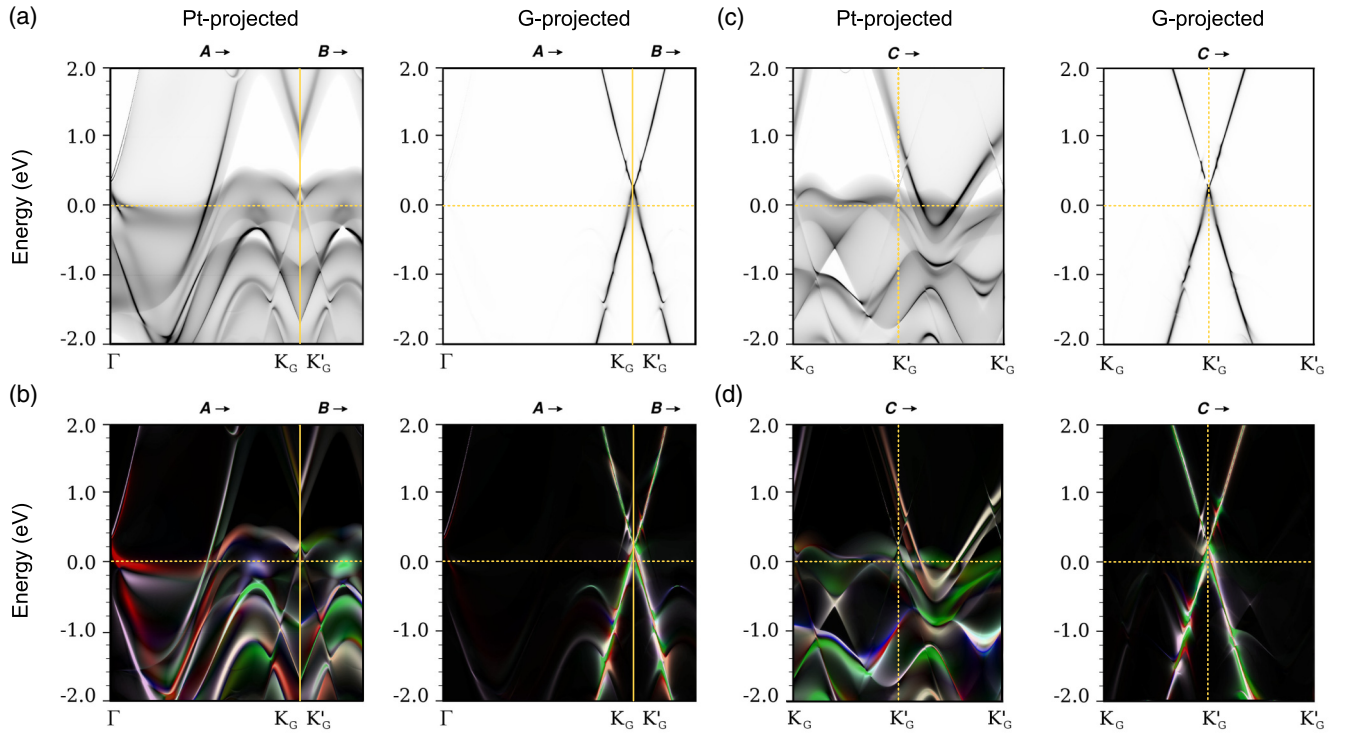

FIG. 6. (a) Left-hand panel: PDOS($\vec{k}$, E) map projected on the Pt surface layer calculated for the G-(3×3)/($\sqrt{7}\times\sqrt{7}$)R19.1° semi-infinite surface and unfolded onto the Pt (1×1) BZ along the k lines A and B indicated in Fig. 1(b). Right-hand panel: Same as (a) but projected and unfolded on the G's primitive BZ. (b) Corresponding magnetization density maps following the same color scheme as in Fig. 5; this time all three components of $\vec{m}(\vec{k}, E)$ are nontrivial. (c) Same as (a) but calculated along path C defined in Fig. 1(b). (d) Spin texture corresponding to the PDOS shown in (c). To view each spin component independently see Figs. S2 and S3 of the Supplemental Material [41].

open at approximately −0.7 and −1.1 eV. Furthermore, despite the complexity of the color scheme employed to visualize $\vec{m}$, spin reorientations can be readily identified throughout.

One must recall, however, that not all the induced streaks and gaps in the DCs can be ascribed to anticrossings with the unfolded metal bands shown in Fig. 5. In the Appendix B we present side by side folded and unfolded G+Pt projections obtained along the same k line (Fig. 11). Due to the BZ backfolding associated to the (2×2) supercell additional Pt bands in other regions of the Pt(111) (1×1) BZ appear in the folded map that, indeed, cross the π bands—also recall the replica of the DC traces visible away from K_G in the Pt-projected maps of Fig. 2.

B. (3×3) phase

Figure 6 summarizes analogous maps calculated for the (3×3) configuration along the paths marked in Fig. 1(b). Since this phase does not present any mirror planes (it belongs to the $p3$ symmetry group), there are no restrictions to the magnetization components. Kramer's degeneracy leads to symmetric PDOS and antisymmetric $\vec{m}$ maps between the $K_G - \Gamma$ and $K'_G - \Gamma$ directions [paths A and B in Fig. 6(b)], while along path C the structure results highly asymmetric. Otherwise, the overall SOC mediated interaction picture is very similar to the previous phase illustrated in Fig. 5. Intense surface states/resonances with well defined magnetizations and oriented along multiple directions (as can be inferred from the highly polychromatic maps) decorate the BZ up to ∼0.5 eV above E_F. Their (anti)crossings with the Dirac cones lead to a blurring of the PDOS and the opening of multiple gaps (notice a particularly large one at −1.5 eV in paths A and B) which transfer a highly complex spin texture to the G states. The upper DC is sharper since only a few Rashba splitted metal sp bands disperse across the empty states region but, still, its spin texture is nontrivial. A sensible difference with the (2×2) case is the larger number of backfolded metal bands that interact with the DCs as a consequence of the larger size of the moiré pattern; indeed, two bands cross this time the previously unperturbed upper cone close to the Dirac point (DP). This fact is highlighted in the folded versus unfolded comparison shown in Appendix B (Fig. 11).

C. SOC induced splittings in the G bands

We complete the G/Pt analysis by presenting in Fig. 7 zooms in of the G projected magnetization maps for both phases and along k paths A and C [left panels (a)–(d)]. Single spectra extracted from these maps at some representative k points are shown in panel (e) (colored lines), including as well the corresponding PDOS(E) curve (gray lines). Let us first consider the anticrossing regions; plots A, D, or G. Here, giant splittings larger than 100 meV can be readily identified in most of the PDOS. The curves comprise up to four peaks, two belonging to the lower edge of the gap and the other two to the upper one. However, since the broadening of each peak can be quite different due to a stronger hybridization of one of the spin components with the metal bands, they are often

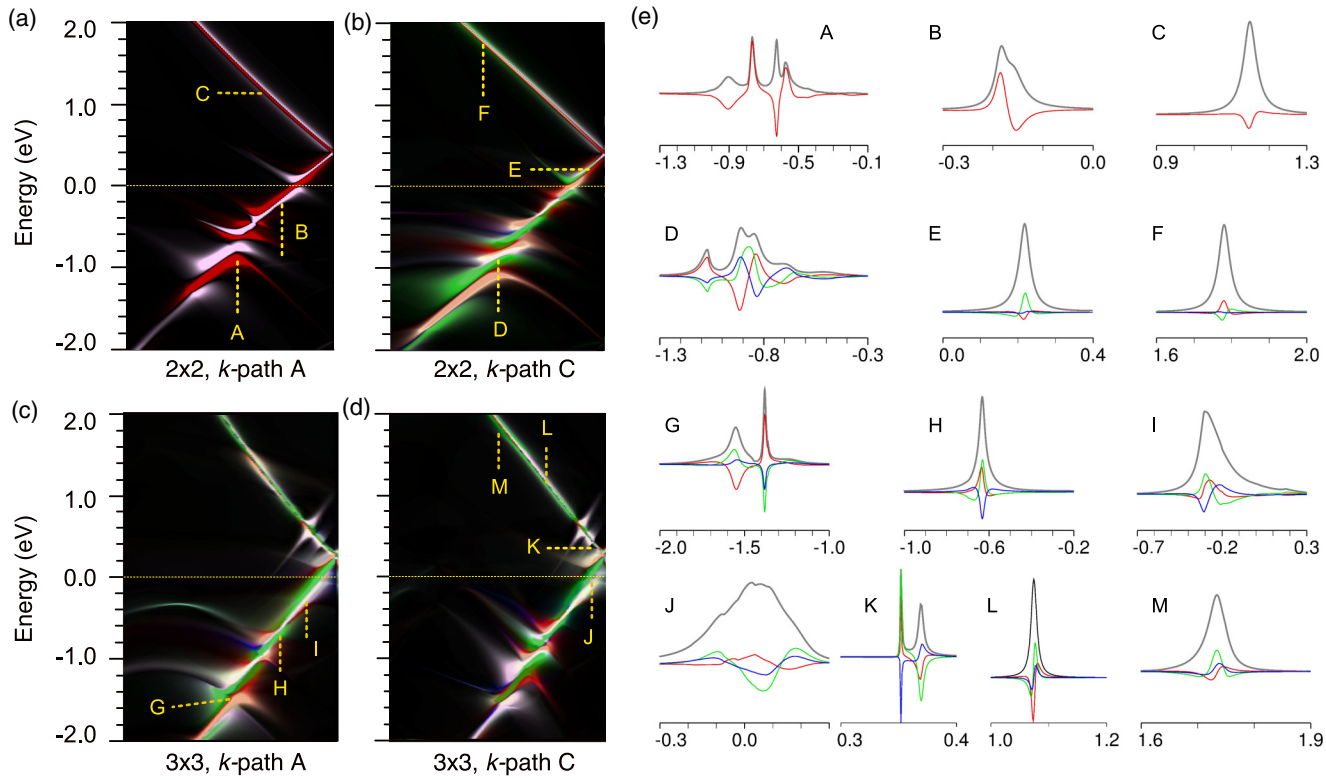

FIG. 7. (a) Zoom in of the G's projected magnetization map in the (2×2) phase presented in the last column of Fig. 2 covering part of the k path A. (b) Same as (a) but for the $\vec{m}(\vec{k}, E)$ map of Fig. 5 (k-path C). (c),(d) Same as (a) and (b) but for the G-magnetization maps of Fig. 6 corresponding to the (3×3) phase. (e) PDOS(E) and $\vec{m}(E)$ single spectra extracted from these maps at specific k points marked with capital letters (A to M) in panels (a)–(d). Gray, red, green, and blue lines represent the PDOS, and $\perp$, $\parallel$ and z components of $\vec{m}$, respectively. Note that the energy ranges considered in the plots can be rather different among them, ranging from 1 eV down to 100 meV while the y axis (not shown) has been rescaled in each plot for the sake of clarity (indeed, the intensity of the sharp peaks at the upper DC tends to be a factor 3–5 larger than in the lower cone).

hard to resolve in the spectra—especially in G. In general, and if not forbidden by symmetry, the three components of the magnetization are nonzero with the spin orientation of each graphene branch depending on that of the metal band causing the anticrossing. It is particularly surprising the emergence of large $m_\parallel$ components (that is, in-plane radial contribution) indicating that no spin-momentum locking at the DCs holds.

To understand the spin rotation process and how the size of the splittings changes between the gap regions let us focus on the sequence of spectra H-I; at H there is a sharp state with $\vec{m} = (+m_\perp, +m_\parallel, -m_z)$ and a broader one with the opposite orientation. Since at this particular k point both are aligned, there is no net splitting. As we move upwards in energy along the lower cone the former broadens and shifts to the left leading to a sizable splitting of ∼100 meV—as may be deduced from the distance between the m_z minimum and maximum. It is also clear that the magnetization changes direction as the band disperses. Other curves acquired at similar quasilinear regions in the lower cone follow a similar pattern (B or E). The fact that their corresponding PDOS show a single (or at most an asymmetric) peak rather than two splitted ones is reminiscent of the resolution achieved in ARPES versus SP-ARPES experiments, since in the former case, typically, no splittings can be resolved in the π bands.

Spectra J and K, taken at the same k point close to the Dirac point, show the drastic transition between the lower and upper cones whereby a single broad and complex peak in the PDOS appears as two sharp maxima splitted by a few tens of meV above E_F. Indeed, in the empty states regions there are hardly any anticrossings and the bands remain sharp and fairly linear (curves C, F, L, and M) while the magnetization does not undergo such abrupt changes (albeit the $m_\parallel$ component is still comparable to the other two). Nevertheless, their splittings become of the order of just 10 meV.

We complete our discussion by comparing the calculated G/Pt properties with the previous ARPES and SP-ARPES results reported by Shikin *et al.* and Klimovskikh *et al.* in Refs. [18,19] for the (2×2) phase as confirmed by the corresponding LEED patterns. Overall, the experiments seem to agree quite well with our maps, especially concerning the hardly perturbed Dirac cones after comparing their spectra against our calculated G's PDOS in Fig. 2(a). Furthermore, the large calculated gap at −0.7 eV matches, within a DFT error of a few hundreds of meV, a pronounced anticrossing between the π bands and the Pt 5d states appearing at around −0.5 eV (Figs. 1(a) and 4(a) in Refs. [18,19]). We also note a discrepancy between the measured and calculated p-doping level; in the above mentioned works the DP is shifted by

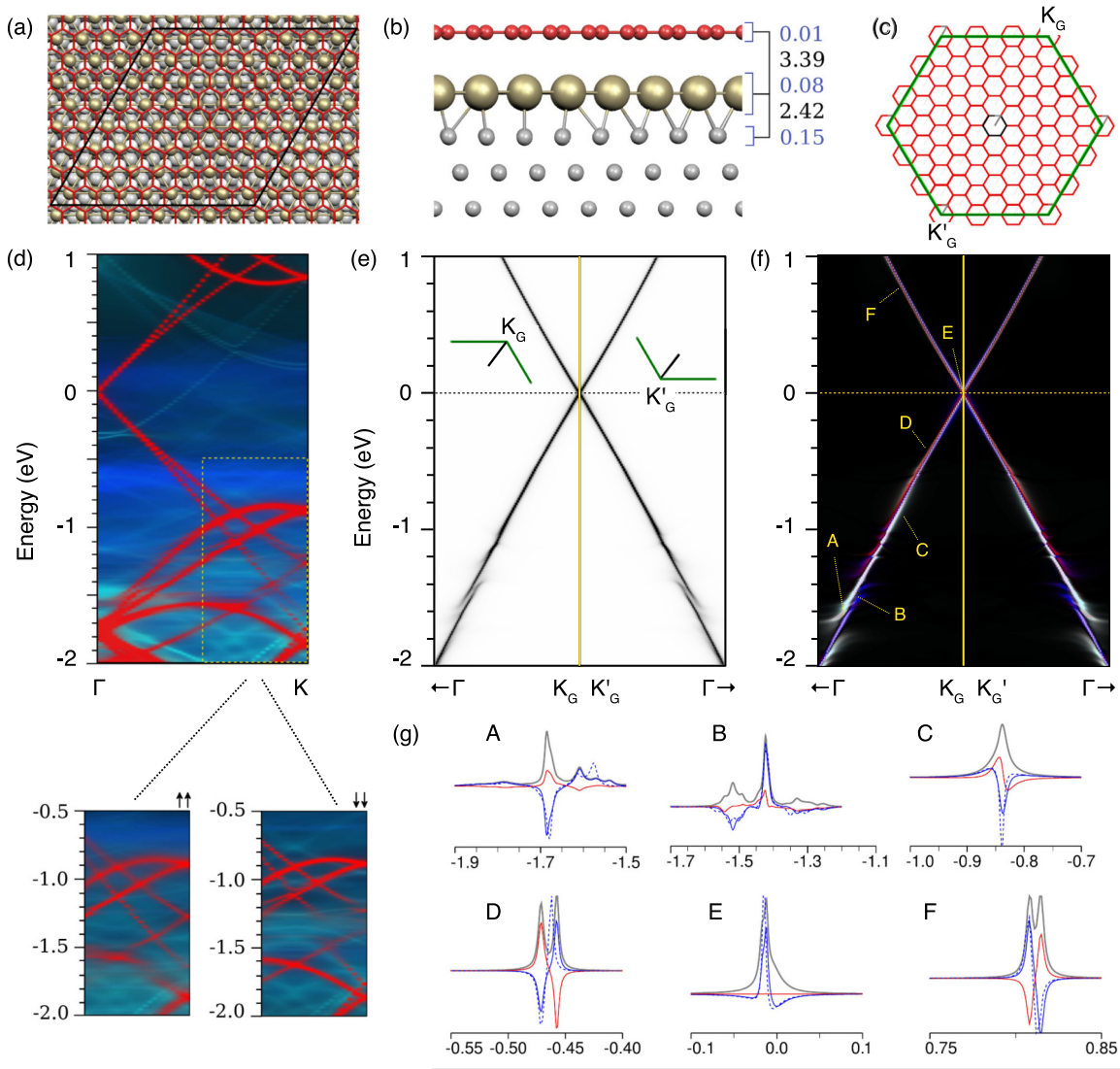

FIG. 8. Top (a) and side (b) views of the G/Au/Ni(111) interface with C, Au, and Ni atoms drawn in red, gold, and gray, respectively. The parallelogram denotes the (9×9)/(8×8)/(9×9) supercell employed. Interlayer average spacings and intralayer corrugations (blue font) are indicated in Å. (c) BZ scheme of the system; black and red small hexagons indicate the supercell's BZ, while the large green hexagon corresponds to the G's (1×1) BZ. Labels with the subindex G refer to the G's primitive BZ. (d) Folded PDOS($\vec{k}$, E) map calculated along the $\Gamma - K - M$ k path indicated by a small solid line in (c) and simultaneously projected on the topmost surface layers of the semi-infinite system: graphene (red), Au (light blue), and the Ni surface (dark blue). The inset below shows the PDOS decomposition into majority and minority spin components (↑↑ and ↓↓ stencils) in the low energy region. (e) PDOS($\vec{k}$, E) projected and unfolded on graphene along a fragment of the $\Gamma - K$ path of the primitive G's BZ. (f) The corresponding magnetization density following the same color scheme as in Fig. 5; only $m_\perp$ and m_z components are present in this case. (g) Single spectra for the PDOS(E) (gray line) and $m_\perp/m_z$ components (red/blue) extracted at selected k points marked in (f). Magnetization curves obtained in the absence of SOC are additionally included in the spectra (blue dashed lines).

100 meV from E_F while in our calculations it is close to 0.4 eV which is, however, only slightly larger than the 0.3–0.4 eV obtained in previous ARPES and STS experiments [37,42] as well as in other DFT studies under different XC functionals [43,44]. Finally, in the light of the magnetization spectra shown in Fig. 7(e), we ascribe the giant splittings (80–200 meV) reported in these experimental works to or close to gap regions where such large values commonly appear. We emphasize, however, that they cannot be interpreted as a standard Rashba shift between the ↑ and ↓ branches of the DCs whereby both spin components would disperse in parallel around E_F. At contrast, the picture that emerges from our simulations is that both the magnetization direction and the splittings undergo continuous changes in k space, while in the linear regions (upper DC), the splittings are not larger than a few tens of meV.

IV. GRAPHENE ON AU/NI(111)

In this section we will focus on the G/Au/Ni(111) system for which we have considered two different interface models based on the related STM study of Jacobsen *et al.* [33]. The first one consists of graphene pseudomorphically grown on an unreconstructed Ni(111) surface with an intercalated Au monolayer between them, which results in a large moiré pattern

involving (9×9) and (8×8) supercells at the G/Ni and Au, respectively [see Fig. 8(a)]—in this configuration the Au-Au intralayer distances are compressed by just 2% with respect to those in the Au-fcc bulk phase. The same commensurate lattice applies to the second model, where the Ni top layer presents a (9×9) reconstruction after removal of five Ni atoms followed by a shift of a ten-atom triangle from *fcc* to *hcp* registry. However, all results for this latter model are presented in Appendix C since, to our surprise, the electronic structure of graphene is hardly modified by such a severe reconstruction. Indeed, the computed adsorption (physisorption) energy is the same for both models (38 meV/C).

After relaxation we found a weak graphene/Au interaction with an uncorrugated G layer located at 3.39 Å above the gold layer [see Fig. 8(b)], slightly larger than the values obtained in previous studies of G/Au interface (3.2–3.3 Å in Refs. [38,39,43,45]), although an eventual error smaller than 0.2 Å should not alter the SOC splittings by more than a few tens of meV [8]. Unexpectedly, the Au layer presents a rather small corrugation of 0.08 Å, similar to that at the Ni topmost layer (0.15 Å). As regards the magnetic properties of the system, the Ni substrate's spin polarization was always set along the surface normal (+z axis) while the intercalated gold was found to couple antiferromagnetically to it with small induced magnetic moments of ~ -0.02 μB/atom versus the $\sim +0.6$ μB/atom at the Ni surface layers and the negligible $+0.002$ μB/atom in graphene.

PDOS($\vec{k}$, E) maps projected on the first atomic layers of the surface are shown in Fig. 8(d). The contributions of G, Au, and Ni are superimposed within the same map each plotted in a different color (red, light blue, and dark blue, respectively). Recall that due to the BZ backfolding which transforms both K_G and K'_G into Γ, the two cones appear superimposed in the figure. This time the linear π bands (red) are almost fully preserved within a ±1 eV interval around E_F, confirming its quasifreestanding character. The intense dark blue horizontal bands centered at around −0.7 and +0.2 eV correspond to the upper part of the majority and minority Ni d bands, respectively. Gold sp bands, including a surface state with onset at −0.33 eV, analogous to the Au(111) Shockley-type L band [29,46], cross the BZ at both positive and negative energies while faint traces of the Au d bands (light blue) appear below −1 eV inducing large distortions in the graphene's π bands. The decomposition of the maps around this region into the diagonal ↑↑ and ↓↓ stencils (majority and minority spin carriers in the absence of SOC) reveals marked differences among them [lower inset in (d)], indicating that the graphene/gold hybridization is spin dependent due to the already exchange-splitted Au states. In particular, the ↓↓ stencil is strongly perturbed around −1.3 eV and the ↑↑ at −1.7 eV.

Figure 8(e) displays the unfolded PDOS($\vec{k}$, E) projected on G along the $\Gamma - K_G/K'_G - \Gamma$ lines of its primitive BZ. The unfolding permits us to disentangle the K_G and K'_G DCs and visualize each π band independently thus allowing a direct comparison versus the experimental ARPES results of Ref. [17]. The corresponding magnetization maps together with some single PDOS and $\vec{m}$ spectra computed at selected k points are shown in panels (f) and (g), respectively. Due to the $p3m$ symmetry holding for the entire surface the PDOS($\vec{k}$, E) map is perfectly symmetric between the $\Gamma - K_G$ and $K'_G - \Gamma$ paths as they are related by a mirror plane. Most notably, the $\vec{m}(\vec{k}, E)$ map displays the same symmetry with a vanishing $m_\parallel$ contribution throughout the entire energy range implying that the in-plane component of the spin remains helical. The fact that m_z does not change sign between the two paths implies that it does not behave as a pseudovector any more but, instead, it is fixed by the magnetic order that completely dominates the out-of-plane spin component over the SOC.

In the lower energy region, the hybridizations with the spin-exchange splitted gold d bands induce streaky features opening several gaps with giant spin splittings larger than 100 meV (curves A and B). The structure of the corresponding spectra shows multiple peaks of different intensity, spin dependent broadenings, and magnetic orientations [always confined within the ($\perp$, z) plane]. This scenario is therefore reminiscent of the strong SOC-mediated interaction found between the G and the Pt-d bands in the previous section. In the ±1 eV range around E_F (curves C, D, E, and F), the lack of hybridizations leads to quasilinear sharp bands which even allow us to resolve the double peak structure in the PDOS(E) in certain cases (D or F). However, the splittings never exceed ∼10 meV. Curve E shows the magnetization at the gapless Dirac point where only m_z is nonzero—i.e., consistent with a weak intrinsic SOC picture. Interestingly, there is a large asymmetry between the two components, the $+m_z$ being much sharper than the $-m_z$.

In order to try to quantify the interplay between SOC and magnetic exchange we have included in the spectra of panel (g) the magnetization in the absence of the former (blue dashed lines). The similarities with the m_z curves (solid blue lines) in all the graphs, even in the distorted regions (curves A or B), reveals that the SOC manifests in this system only as a rather small perturbation to the electronic structure, its main effect being the emergence of an in-plane helical component, $m_\perp$, in the spin texture (solid red lines).

Figure 9 presents constant energy $\vec{m}(\vec{k})$ surfaces computed around K_G at several energies above and below the Dirac point, as sketched at the central panel. The circular features become more trigonally distorted as the energy is further away from the Dirac point. The in-plane projections $m_{x/y}$ make patent the helical character of the π states as well as a small RS since the DCs appear k shifted with respect to each other (as expected, the shifts are along the same directions in the upper and lower cones). On the other hand, the m_z maps do not follow a standard exchange magnetic picture whereby the entire band structure of each spin branch would be shifted in energy (vertically) with respect to the other one. Here, the upper cone couples ferromagnetically (dark/minority circles lie inside the white/majority ones) and the lower cone antiferromagnetically to the Au/Ni substrate. The only exception is the −100 meV map where the broad minority band appears at both sides of the sharper majority circle.

Last, we discuss the agreement between our results and the experimental data obtained via ARPES and SP-ARPES reported in Refs. [16,17]. Our calculations reproduce well the quasifreestanding character of the G on this surface, as the DCs appear rather intact (within the energy interval considered in our work), as well as the negligible doping and the absence of a gap at the Dirac point. Furthermore, the kink observed

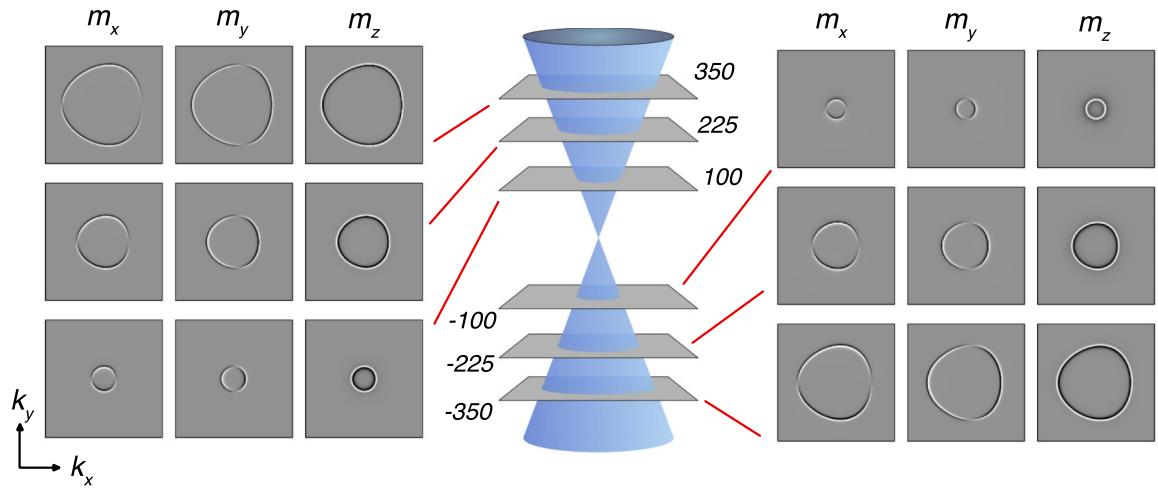

FIG. 9. Unfolded G-projected $\vec{m}(\vec{k})$ maps calculated at selected values of energy and within k regions of the Dirac cones (see sketch in the middle panel with the energies given in meV). Left-hand (right-hand) panel displays the energy cuts at the upper (lower) Dirac cones. The $x/y/z$ components of $\vec{m}$ are plotted separately in the first/second/third column of each panel employing a grayscale color scheme with positive (negative) values of magnetization drawn in white (black).

at −0.95 eV in Ref. [16] and ascribed to an electron-mass renormalization in the DC's dispersion matches well with the onset of strong perturbations in the π bands which in our simulations appear below −1 eV. In fact, if a straight line taken along the upper DC in Fig. 8(e) is extrapolated towards negative energies (not shown), deviations from the lower cone appear around this onset and in the same direction as the experiments (towards a smaller electron mass). Finally, our calculated splitting values (of around 10 meV) perfectly agree with those derived in the first SP-ARPES study (13 ± 3 meV), although we attribute their origin to the magnetic order rather than to a Rashba-type SOC which, anyhow, is observable in our simulations. On the other hand, our results cannot explain the giant (∼100 meV) splittings measured in Ref. [17] for one of the two phases that coexisted within the same surface and attributed to a possible corrugation of the G layer which could lead, locally, to unusually small G/Au distances. Our simulations employing a realistically large supercell seem to exclude this possibility since the G is found to be only weakly physisorbed and remains hardly corrugated even after the large surface reconstruction described in Appendix C. A possible alternative explanation could be the formation of a Ni/Au alloy at the surface layer which could bring the G closer to the surface due to the stronger G-Ni coupling, as has been recently proved for the G/Fe/Ir(111) system [47]. Still, and based on the results presented here, we believe that giant splittings will not show up in the quasilinear regions but only at anticrossings (gaps) that could emerge close to E_F due to the presence of Ni atoms at the top layer [48].

V. SUMMARY AND CONCLUSIONS

In summary, we have unveiled with unprecedented detail the SOC-induced spin texture in the graphene's π bands arising from the presence of a heavy metal semi-infinite substrate. We have considered two paradigmatic systems: a nonmagnetic Pt(111) and a spin-polarized Au/Ni(111) surface. For the former we find that the SOC splitted continuum of metal bands hybridize with the Dirac cones at multiple energies and manifest as local spin-dependent deformations in the linear bands at the avoided crossing gaps, often exceeding 100 meV, accompanied by spin reorientations at the edges, while in between gaps (quasilinear regions) a reduced splitting of at most 10–20 meV remains. Both the precise value of the splitting as well as the G's induced magnetization change continuously as the splitted branches disperse, typically crossing between them and bearing different widths. Therefore, we conclude that the giant SO splittings reported for this system are most probably located close to anticrossing gaps. The number and energy location of the avoided crossings will in general depend on the particular moiré pattern since, as the metal BZ shrinks or rotates with respect to that of graphene, different metal bands will mix [see the comparison between the (2×2)- and (3×3)-G/Pt phases in Fig. 11]. Obviously, as the supercell (moiré pattern) increases in size further crossings will be expected leading to even more complex spin texture.

In the case of G/Au/Ni(111), the absence of gold d states around the Fermi level leaves continuous linear π branches with small splittings in the 10 meV range. However, their origin is mainly the substrate's magnetic order that is transferred to graphene, while the induced SOC introduces a helical in-plane component to the magnetization but hardly alters the G's total PDOS. No evidence for large RSs of the Dirac cones in this energy region was found for either of the two different phases considered, at contrast with a previous experimental study [17]; we assign this discrepancy to a possible Au/Ni alloying process at the surface layer. The presence of Au-d states below −1 eV, on the other hand, leads again to a complex spin structure similar to that found for both G/Pt phases.

We note that unveiling such a complex spin texture represents a key finding which not only opens a new challenge to current (SP-)ARPES based studies of the SO proximity effect, but should also stimulate further research aiming at engineering the *relativistic* electron's spin. Indeed, there are several non-negligible problems to be solved. On one hand, splitting the two spin branches by sizable energies (>100 meV)

seems only possible at anticrossing regions with the metal's d states where the π bands lose their linear character as gaps are opened and therefore electronic transport across the G layer is suppressed. Furthermore, no spin-momentum locking holds in these regions as the G's induced magnetization acquires very different orientations in space depending on the specific metal band with which it hybridizes. On the other hand, at quasilinear regions, either in between these gaps or where no d bands are present (typically the upper DC), only very small splittings ($<kT$) can be observed, with the further disadvantage that the two branches do not necessarily disperse strictly parallel and may even cross yielding an interchange of magnetizations. The broadening induced by the substrate's self-energy is also found to be highly relevant in the G's final spin texture, as it strongly varies between the two spin components often leading to single sharp peaks emerging from a broader background signal.

Our results show a tradeoff between large SOC-derived splittings and the loss of linearity of the π bands, which needs to be overcome in order to harness the SOC-induced magnetization. We believe, however, that our detailed analysis of the spin-orbit proximity effect in graphene adsorbed on metallic substrates, far beyond the resolution of current photoemission techniques, will not only motivate further experimental studies aiming to capture the G's spin properties, but will also facilitate their correct interpretation. Moreover, it remains to address any topological properties that could emerge at the multiple gaps opened. Intrinsic SOC transferred to the G via the proximity effect is known to induce a QSHE state after small gap openings (of at most a few tens of meV) at the Dirac point [13] while here much larger gaps (100–200 meV) have been systematically found away from K_G often crossed by a nonvanishing density of states.

ACKNOWLEDGMENTS

We are deeply grateful to Prof. A. Arnau for the critical reading of the manuscript and his highly stimulating comments. J.S. acknowledges Polish Ministry of Science and Higher Education for financing the postdoctoral stay at the ICMM-CSIC in the frame of the program Mobility Plus (Grant No. 910/MOB/2012/0). J.I.C acknowledges support from the Spanish Ministry of Economy and Competitiveness under Contract No. MAT2015–66888-C3-1R.

APPENDIX A: BRILLOUIN ZONE UNFOLDING

In the case of moiré patterns (or supercells in general), where lattices at layers I and J are different and a common supercell S exists for both, any $\vec{k}$ point within the BZ of layer I, $\vec{k}_I$, may be expressed as $\vec{k}_I = \vec{k}_S + \vec{G}_I$, where $\vec{k}_S$ is confined within the BZ of S and $\vec{G}_I$ are the so-called $\vec{G}$ vectors [24] that relate the reciprocal lattices of S and I; the number of these vectors is given by the ratio between the unit cell areas of S and I, N_{SI} (see Fig. 10). Since for the combined system only $\vec{k}_S$ is conserved, any quantity in k space projected at layer I will mix all $\vec{G}_I$ vectors (BZ folding). However, when the I-J interaction is weak, one may expect that, to a good approximation, translation symmetry is preserved at layer I and hence, $\vec{k}_I$ is approximately conserved within this layer. We explain below in detail our procedure to obtain such unfolded band structure from a supercell slab calculation.

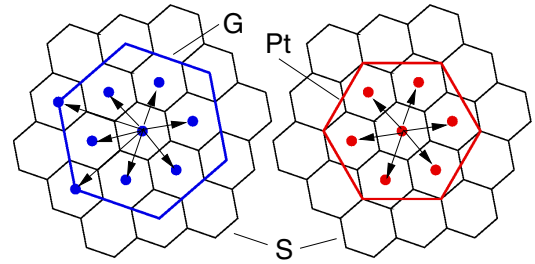

FIG. 10. BZ schemes for the G-(3×3) lattice (blue hexagon in left-hand figure), the Pt-($\sqrt{7}\times\sqrt{7}$)R19.1° (red in right-hand figure), and their commensurate cell S (black hexagons in both figures). The $\vec{G}$ vectors pointing to the S BZs enclosed by the G and Pt BZs (9 and 7, respectively) are indicated by the arrows (apart from the Γ point $\vec{G} = 0$).

Considering the general case where the substrate's unit cell is the same as that of the supercell S (i.e., a reconstructed surface) and denoting by the index I the graphene layer adsorbed on top whose electronic structure we wish to unfold, we first construct the intralayer Hamiltonian in k space as:

$$H_{II}(\vec{k}_I) = \frac{1}{N_{SI}} \sum_{\vec{R}_I,\vec{L}_I} e^{i\vec{k}_I(\vec{R}_I-\vec{L}_I)} H_{II}(\vec{R}_I - \vec{L}_I), \qquad \text{(A1)}$$

where $\vec{R}_I$ runs over the lattice vectors at I, $\vec{L}_I$ are the vectors linking the origin of the layer with that of each of the N_{SI} unit cells contained in the S supercell, and $H_{II}(\vec{R}_I - \vec{L}_I)$ contains the matrix elements between the G's unit cell centered at $\vec{L}_I$ and those shifted by $\vec{R}_I$—all of them available from the self-consistent slab's Hamiltonian previously computed and saved. Equation (A1) thus averages the matrix elements between the carbon A and B atoms over the entire supercell so that translational symmetry is *imposed* within the layer. Next, we express the k-space interactions between I and S as:

$$H_{IS}(\vec{k}_S, \vec{G}_I) = \frac{1}{\sqrt{N_{SI}}} \sum_{\vec{R}_S,\vec{L}_I} e^{i(\vec{k}_S+\vec{G}_I)(\vec{R}_S-\vec{L}_I)} H_{IS}(\vec{R}_S - \vec{L}_I), \qquad \text{(A2)}$$

where, again, all interlayer $H_{IS}(\vec{R}_S - \vec{L}_I)$ matrix elements can be extracted from the self-consistent supercell slab calculation. The Green's function projected at layer I may then be expressed according to:

$$G_{II}(\vec{k}_S, \vec{G}_I, E) = \left(F_{II}(\vec{k}_I, E) + \Sigma^S_{II}(\vec{k}_S, \vec{G}_I, E)\right)^{-1}, \qquad \text{(A3)}$$

where $F = E \cdot O - H$ is the secular matrix and $\Sigma^S_{II}(\vec{k}_S, \vec{G}_I)$ stands for the self-energy at layer I arising from the presence of the substrate, which may be calculated via Green's functions techniques following the same k scheme as for $H_{IS}(\vec{k}_S, \vec{G}_I)$ [25]. Unfolding the BZ at I may now be easily carried out by extracting the contribution of each $\vec{k}_I = \vec{k}_S + \vec{G}_I$ term individually. In practice, we run $\vec{k}_I$ along a given direction and only retain the $\vec{G}_I = 0$ contribution of $G_{II}(\vec{k}_S, \vec{G}_I, E)$.

Similar to the case of G, BZ unfolding may also be performed for any substrate layer as long as it is not strongly reconstructed. The above procedure remains valid, although for the surface layer we need to consider two interlayer interactions (self-energies) instead of just one: that involving the G and that with the rest of the substrate below. In general, to reduce the number of approximations associated to this approach we

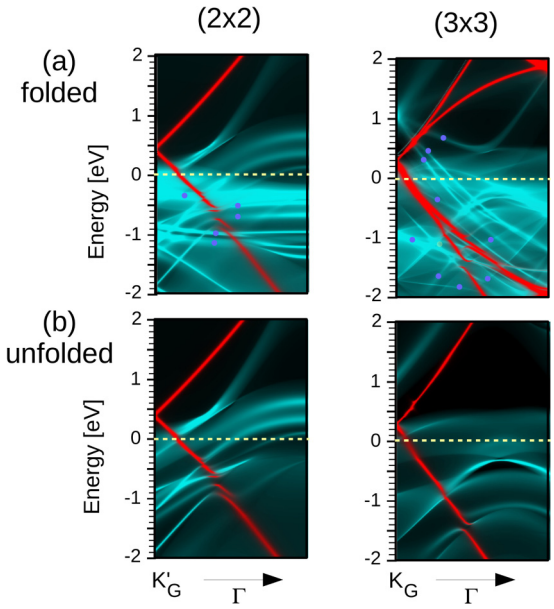

FIG. 11. DOS($\vec{k}$, E) maps projected on the G (red) and first Pt layer (light blue) calculated for the G/Pt (2×2) (left column) and (3×3) (right column) phases along the B k paths shown in Fig. 1. (a) Unfolded band structure after assuming that the (1×1) translational symmetry is preserved at the G and surface Pt layers (see Appendix A) and, (b) folded band structure employing the $(2\times2)/(\sqrt{3}\times\sqrt{3})R30^\circ$ and $(3\times3)(\sqrt{7}\times\sqrt{7})R19.1^\circ$ supercells to describe all G/Pt layers.

perform the unfolding for the G and the surface metal layer in separate calculations.

Let us finally note that our unfolding scheme is exact as long as translational symmetry is strictly preserved at layer I. For the quasifreestanding G case, either on Pt(111) or Au/Ni(111), the G-metal interactions are indeed weak and it is clearly a good approximation.

APPENDIX B: G/PT(111) FOLDED BAND STRUCTURES

In Fig. 11 we present a comparison of the folded (top panels) versus unfolded (bottom panels) PDOS($\vec{k}$, E) maps for both the G/Pt (2×2) and (3×3) phases computed along the $K'_G - \Gamma$ direction [k paths B in Fig. 1(b)]. We have simultaneously merged in each map the G (colored in red) and first Pt layer (light blue) projections. For the (2×2) phase (left column) around five new backfolded Pt bands appear below E_F and cross the G's π band (each marked by a small blue circle), while the upper cone remains identical to that of the unfolded case due to the absence of extra bands. The profusion of backfolded Pt bands is much larger in the (3×3) phase, as should be expected due to its smaller BZ size. In this geometry both DCs (K_G and K'_G) are backfolded into the Γ point and hence, the two branches appear superimposed in the upper map. We have again marked with small circles those which do not appear in the unfolded map (up to eight clearly visible) with the peculiarity that this time, two of them cross the upper DC inducing the small distortions around 0.6 eV that can be appreciated in the unfolded map below.

APPENDIX C: G/AU/NI(111) RECONSTRUCTED MODEL

We describe here the results for an alternative G/Au/Ni(111) model, whose geometry differs from the one considered in the main text by the Ni substrate's reconstruction, based on

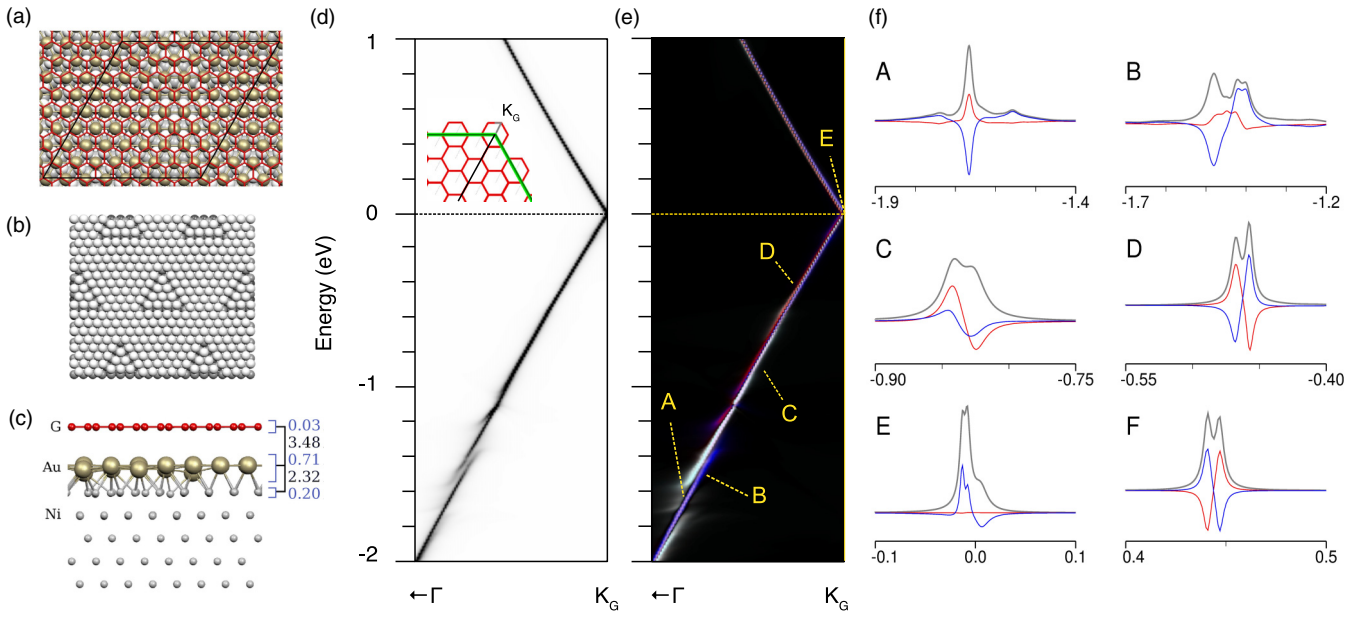

FIG. 12. (a)–(c) Top and side views of the relaxed geometry for the reconstructed G/Au/Ni(111) configuration. C, Au, and Ni atoms are drawn as red, gold, and gray balls, respectively. In (b) the Au and G layers have been removed in order to show the Ni triangular motif characteristic of this reconstruction. In (c) first interlayer average spacings (black font) and intralayer corrugations (blue font) are indicated in Å. (d) Electronic structure and (e) corresponding magnetization density unfolded and projected on graphene along the $\Gamma - K_G$ line of its primitive BZ (shown in the inset). Color scheme same as in the maps shown in the main paper. (f) Single spectra extracted from panels (d) and (e) at the k points marked in the latter; PDOS(E) in solid gray and $m_{\perp/z}(E)$ components in red/blue (the $m_\parallel$ is zero along this k line).

previous STM studies [33] where the deposition of Au on Ni(111) at RT yielded a complex $\sim(9.7\times9.7)$ reconstruction with triangular motifs assigned to a strongly reconstructed top Ni layer whereby five vacancies are created and ten surface Ni atoms forming a triangle are shifted from an fcc to an hcp registry [see Fig. 12(b)] [33,49]. Although there is no experimental evidence for the existence of such a configuration when graphene is deposited on top, we have considered it as a possible explanation for the appearance of two phases with different splittings as reported in the SP-ARPES experiments [17].

In Figs. 12(a)–12(c) we summarize the relaxed geometry of such a configuration; for simplicity, we have assumed the same G/Au/Ni $(9\times9)/(8\times8)/(9\times9)$ commensurate supercell as for the unreconstructed model since it can nicely accommodate the large triangular motifs. Although the triangular Ni motifs induce a large buckling in the Au layer of 0.7 Å, the corrugation of graphene remains negligible (0.03 Å) with an average G-Au distance of $d_{G-M} = 3.48$ Å only slightly larger than in the unreconstructed model considered in the main text. The Au layer again exhibits a small magnetic moment of 0.03 μB/atom antiferromagnetically coupled to that of the Ni surface. Figures 12(d)–12(f) present the unfolded PDOS($\vec{k}$, E) and magnetization maps together with single spectra extracted from the latter, following the same scheme as in Fig. 8. The maps corresponding to the unreconstructed and reconstructed phases are qualitatively very similar, with an almost intact (only weakly spin-splitted) upper Dirac cone and the lower cone strongly textured due to multiple hybridizations with the metal bands particularly below -1 eV. At the Dirac point (spectra E), two overlapping peaks can be seen signaling a larger intrinsic SOC for this model, although their broadenings, different for each spin, are both sufficiently large to close any gap. Nevertheless, and as can be seen from the single spectra in panel (f), the magnitude of the spin splittings along the DC do not exceed a few tens of meV in the quasilinear regions. Therefore, and similar to the unreconstructed model described in the main text, the triangular surface reconstruction cannot explain either the giant RS splitting phase recently reported for this system [17].

[1] W. Han, R. K. Kawakami, M. Gmitra, and J. Fabian, Nat. Nanotechnol. **9**, 794 (2014).
[2] J. Balakrishnan, G. K. W. Koon, A. H. C. Neto, and B. Ozyilmaz, Nat. Phys. **9**, 284 (2013).
[3] J. Balakrishnan, G. K. W. Koon, A. Avsar, Y. Ho, J. H. Lee, M. Jaiswal, S.-J. Baeck, J.-H. Ahn, A. Ferreira, M. A. Cazalilla, A. H. C. Neto, and B. Ozyilmaz, Nat. Commun. **5**, 4748 (2014).
[4] C. L. Kane and E. J. Mele, Phys. Rev. Lett. **95**, 226801 (2005).
[5] W.-K. Tse, Z. Qiao, Y. Yao, A. H. MacDonald, and Q. Niu, Phys. Rev. B **83**, 155447 (2011).
[6] Z. Qiao, S. A. Yang, W. Feng, W.-K. Tse, J. Ding, Y. Yao, J. Wang, and Q. Niu, Phys. Rev. B **82**, 161414(R) (2010).
[7] E. McCann and V. I. Fal'ko, Phys. Rev. Lett. **108**, 166606 (2012).
[8] F. Calleja, H. Ochoa, M. Garnica, S. Barja, J. J. Navarro, A. Black, M. M. Otrokov, E. V. Chulkov, A. Arnau, A. L. Vazquez de Parga, F. Guinea, and R. Miranda, Nat. Phys. **11**, 43 (2015).
[9] M. Gmitra, S. Konschuh, C. Ertler, C. Ambrosch-Draxl, and J. Fabian, Phys. Rev. B **80**, 235431 (2009).
[10] S. Konschuh, M. Gmitra, and J. Fabian, Phys. Rev. B **82**, 245412 (2010).
[11] A. Avsar, J. Y. Tan, T. Taychatanapat, J. Balakrishnan, G. Koon, Y. Yeo, J. Lahiri, A. Carvalho, A. S. Rodin, E. O-Farrell, G. Eda, A. H. C. Neto, and B. Ozyilmaz, Nat. Commun. **5**, 4875 (2014).
[12] S. Irmer, T. Frank, S. Putz, M. Gmitra, D. Kochan, and J. Fabian, Phys. Rev. B **91**, 115141 (2015).
[13] C. Weeks, J. Hu, J. Alicea, M. Franz, and R. Wu, Phys. Rev. X **1**, 021001 (2011).
[14] M. Gmitra and J. Fabian, Phys. Rev. B **92**, 155403 (2015).
[15] M. Kralj, Nat. Phys. **11**, 11 (2015).
[16] A. Varykhalov, J. Sanchez-Barriga, A. M. Shikin, C. Biswas, E. Vescovo, A. Rybkin, D. Marchenko, and O. Rader, Phys. Rev. Lett. **101**, 157601 (2008).
[17] D. Marchenko, A. Varykhalov, M. Scholz, G. Bihlmayer, E. Rashba, A. Rybkin, A. Shikin, and O. Rader, Nat. Commun. **3**, 1232 (2013).
[18] A. M. Shikin, A. A. Rybkina, A. G. Rybkin, I. I. Klimovskikh, P. N. Skirdkov, K. A. Zvezdin, and A. K. Zvezdin, Appl. Phys. Lett. **105**, 042407 (2014).
[19] I. I. Klimovskikh, S. S. Tsirkin, A. G. Rybkin, A. A. Rybkina, M. V. Filianina, E. V. Zhizhin, E. V. Chulkov, and A. M. Shikin, Phys. Rev. B **90**, 235431 (2014).
[20] I. I. Klimovskikh, O. Vilkov, D. Y. Usachov, A. G. Rybkin, S. S. Tsirkin, M. V. Filianina, K. Bokai, E. V. Chulkov, and A. M. Shikin, Phys. Rev. B **92**, 165402 (2015).
[21] A. Varykhalov, J. Sanchez-Barriga, D. Marchenko, P. Hlawenka, P. Mandal, and O. Rader, Nat. Commun. **6**, 7610 (2015).
[22] I. I. Klimovskikh, M. M. Otrokov, V. Y. Voroshnin, D. Sostina, L. Petaccia, G. Di Santo, S. Thakur, E. V. Chulkov, and A. M. Shikin, ACS Nano **11**, 368 (2017).
[23] O. Rader, A. Varykhalov, J. Sánchez-Barriga, D. Marchenko, A. Rybkin, and A. M. Shikin, Phys. Rev. Lett. **102**, 057602 (2009).
[24] J. Cerdá, M. A. Van Hove, P. Sautet, and M. Salmeron, Phys. Rev. B **56**, 15885 (1997).
[25] E. T. R. Rossen, C. F. J. Flipse, and J. I. Cerdá, Phys. Rev. B **87**, 235412 (2013).
[26] J. M. Soler, E. Artacho, J. D. Gale, A. Garcia, J. Junquera, P. Ordejon, and D. Sanchez-Portal, J. Phys.: Condens. Matter **14**, 2745 (2002).
[27] J. P. Perdew, K. Burke, and M. Ernzerhof, Phys. Rev. Lett. **77**, 3865 (1996).
[28] F. Ortmann, F. Bechstedt, and W. G. Schmidt, Phys. Rev. B **73**, 205101 (2006).
[29] R. Cuadrado and J. I. Cerdá, J. Phys.: Condens. Matter **24**, 086005 (2012).
[30] M. Gao, Y. Pan, L. Huang, H. Hu, L. Z. Zhang, H. M. Guo, S. X. Du, and H.-J. Gao, Appl. Phys. Lett. **98**, 033101 (2011).
[31] M. Enachescu, D. Schleef, D. F. Ogletree, and M. Salmeron, Phys. Rev. B **60**, 16913 (1999).
[32] P. Merino, M. Svec, A. L. Pinardi, G. Otero, and J. A. Martin-Gago, ACS Nano **5**, 5627 (2011).

[33] J. Jacobsen, L. P. Nielsen, F. Besenbacher, I. Stensgaard, E. Laegsgaard, T. Rasmussen, K. W. Jacobsen, and J. K. Nørskov, Phys. Rev. Lett. **75**, 489 (1995).
[34] G. Mercurio, E. R. McNellis, I. Martin, S. Hagen, F. Leyssner, S. Soubatch, J. Meyer, M. Wolf, P. Tegeder, F. S. Tautz, and K. Reuter, Phys. Rev. Lett. **104**, 036102 (2010).
[35] R. Cuadrado, J. I. Cerda, Y. Wang, G. Xin, R. Berndt, and H. Tang, J. Chem. Phys. **133**, 154701 (2010).
[36] C. Rogero, J. A. Martin-Gago, and J. I. Cerdá, Phys. Rev. B **74**, 121404 (2006).
[37] P. Sutter, J. T. Sadowski, and E. Sutter, Phys. Rev. B **80**, 245411 (2009).
[38] T. Olsen and K. S. Thygesen, Phys. Rev. B **87**, 075111 (2013).
[39] J. Slawinska, P. Dabrowski, and I. Zasada, Phys. Rev. B **83**, 245429 (2011).
[40] R. Mazzarello, A. D. Corso, and E. Tosatti, Surf. Sci. **602**, 893 (2008).
[41] See Supplemental Material at http://link.aps.org/supplemental/10.1103/PhysRevB.98.075436 for separate maps for each spin projection.
[42] M. M. Ugeda, D. Fernandez-Torre, I. Brihuega, P. Pou, A. J. Martinez-Galera, R. Pérez, and J. M. Gómez-Rodriguez, Phys. Rev. Lett. **107**, 116803 (2011).
[43] P. A. Khomyakov, G. Giovannetti, P. C. Rusu, G. Brocks, J. van den Brink, and P. J. Kelly, Phys. Rev. B **79**, 195425 (2009).
[44] J. Slawinska and I. Zasada, Phys. Rev. B **84**, 235445 (2011).
[45] J. Slawinska, I. Wlasny, P. Dabrowski, Z. Klusek, and I. Zasada, Phys. Rev. B **85**, 235430 (2012).
[46] S. LaShell, B. A. McDougall, and E. Jensen, Phys. Rev. Lett. **77**, 3419 (1996).
[47] J. Brede, J. Slawinska, M. Abadia, C. Rogero, J. E. Ortega, I. Piquero-Zulaica, J. Lobo-Checa, A. Arnau, and J. I. Cerda, 2D Mater. **4**, 015016 (2017).
[48] Y. S. Dedkov and M. Fonin, New J. Phys. **12**, 125004 (2010).
[49] F. Besenbacher, Rep. Prog. Phys. **59**, 1737 (1996).